Ce Doping Boosts the Thermo- and Photocatalytic Oxidation of CO at Low Temperature in TiZrO$_4$ Solid Solutions

Panjuan Tang, Stefano Livraghi, Elio Giamello, Sebastiano Garroni, Luca Malfatti, and Stefano Agnoli*

Palladium nanoparticles supported on zirconium titanate with cerium doping up to 10% molar (Ce-ZT) are prepared by a facile impregnation method and characterized by several techniques. Due to electronic effects, the amount of Ce cations in a reduced oxidation state, i.e., Ce(III), is surprisingly high, more than 50% of the total cerium amount. The Pd decorated Ce-ZT nanoparticles exhibit excellent catalytic activity in the low temperature oxidation of CO. The amount of Pd and Ce concentration results to be the key parameters controlling the catalytic performance. The best activity is observed in the sample with the highest Ce doping (10% molar) and a nominal Pd loading of 2% w/w, which exhibits an outstanding turnover frequency of 0.1 s^{-1} at 45 °C. Moreover, the CO conversion remains unchanged at 100% for 24 h at 50 °C, or for several successive light-off experiments up to 120 °C, demonstrating excellent long-term stability. Light irradiation is shown to further improve the catalytic performance allowing to reach the same catalytic activity of dark conditions at a temperature that is 20–40 °C lower. Electron paramagnetic resonance spectroscopy experiments indicate that Pd nanoparticles and Ce(III) ions can trap electrons favoring charge separation and formation of superoxide species, therefore enabling photocatalysis.

1. Introduction

Carbon monoxide is a high-risk toxic gas that is a common by-product of the oxidation of organic compounds. Because of the continuous growth of the industry and development of motor vehicle transportation, the undesired emission of CO in the environment has become a serious worldwide concern. This gas is colorless, odorless, and with a density close to that of air, so it is rather hard to notice when its concentration raises in the ambient. Moreover, the toxic effects of this gas can be observed even at very low concentrations (10–24 ppm), therefore it is rather important to find efficient ways for the elimination of CO from the environment. Up to now, there are two main methods to achieve this goal: physical adsorption and chemical conversion. The physical adsorption method mainly uses a porous material with a high specific surface area to adsorb CO through intermolecular van der Waals forces; however, CO can eventually escape from the material and be released in the atmosphere again.[1] On the other hand, chemical conversion and especially catalytic oxidation offer a more permanent solution to the CO elimination by producing an inert and nontoxic compound such as CO$_2$.[2] However, to be truly environmentally friendly, the chemical processes involved in the CO conversion must be energy efficient and involve sustainable materials. This calls for the development of novel catalysts either capable to work at low temperature or that can exploit easily available energy sources such as sunlight (i.e., photocatalysis).[3]

Traditionally, the best catalysts for CO oxidation are a combination of an active metal and a metal oxide.[4] In general, the first component is necessary to bind CO, whereas the second one can be either involved in the oxygen activation or act as a promoter of the activity of the metal through a variety of electronic or structural effects.[5] Noble metals clearly demonstrated to be the best option among metal phases and palladium in particular has been in the spotlight of research since the seminal work by Arrii and co-workers.[6] In the course of years, a wide gamut of oxide supports has been investigated, ranging from materials with highly complex composition or special structure and morphology; anyway despite the variety of results it turns out that the best performances are obtained by reducible

Dr. P. Tang, Prof. S. Agnoli
Department of Chemical Sciences
University of Padova
Via F. Marzolo 1, Padova 35131, Italy
E-mail: stefano.agnoli@unipd.it

Prof. S. Livraghi, Prof. E. Giamello
Dipartimento di Chimica and NIS
Università di Torino
Via P. Giuria 7, Torino 10125, Italy

Dr. S. Garroni, Prof. L. Malfatti
Laboratorio di Scienza dei Materiali e Nanotecnologie
CR-INSTM
Dipartimento di Chimica e Farmacia
Università di Sassari
Via Vienna 2, Sassari 07100, Italy

oxides such as CeO_2, TiO_2, ZrO_2, FeO_x, CoO_x, MnO_x, WO_3, or more complex binary oxides such as $BaTiO_3$, $LaCoO_3$.[7] In this context ceria has a special place both scientifically and technologically, considering both the extremely prolific and steady research activity devoted to this material, and its technological application. Ceria, together with Pd, is widely used in three way catalysts, which represent the most important devices in the market, which exploit the CO oxidation.[8]

One of the key features of ceria, which is common to the large family of reducible oxides, is the ability to either form or eliminate oxygen vacancies quite easily, and this feature is at the basis of important phenomena such as high oxygen storage capacity, advanced oxidation redox properties, high ionic conductivity.[9] The formation of an oxygen vacancy in CeO_2 implies the removal of one oxygen from the anion lattice of the oxide and the consequent reduction of two Ce(IV) ions to Ce(III) ions. Lawrence et al. demonstrated that the catalytic activity in the CO oxidation is a function of the concentration of oxygen vacancies,[10] and in general oxygen vacancy formation energy is considered one of the best descriptor of the catalytic activity in the CO oxidation reaction. Therefore many strategies have been envisaged to maximize this type of defects. Among these, there are the introduction of dopants,[11] the formation of mixed phases with other oxides,[12] or the control of shape and dimensions,[13] and the exploitation of electronic effects.[12d,14]

In the present paper, we used a relatively new class of materials consisting of solid solution of TiO_2 and ZrO_2, which were doped with ceria. $ZrTiO_4$ (hereafter named ZT) can not only maintain the original special properties of TiO_2 and ZrO_2, such as chemical and mechanical stability, tunable acid/base Bronsted/Lewis properties, but also overcome their respective shortcomings, such as tendency to sinter and low activity at low temperature. In recent years, $ZrTiO_4$ composite oxides have become a research hotspot due to their special chemical properties and have been used for a variety of chemical processes such as isopropanol dehydration,[15] salicylic acid photo-oxidation, and Cr (VI) photoreduction.[16]

The doping of $ZrTiO_4$ with cerium (forming the systems hereafter labeled as Ce_x-ZT, where x indicates the molar fraction of Ce) has been recently studied by some of us.[17] It has been demonstrated that cerium cations can be substitutionally introduced in the lattice of the zirconium titanate up to a level

of 10 mol%. Interestingly, theoretical calculations and X-ray photoelectron spectroscopy (XPS) data indicated that the empty Ce 4f levels are lower in energy than the Ti 3d and Zr 4d bands, allowing an easy and selective formation of reduced Ce^{3+} species. Moreover, the doping with cerium imparts the material with an increased optical absorption in the visible range, whereas surface exposed Ce^{3+} cations can adsorb molecular oxygen and easily transfer an electron to it, forming superoxides species. The combination of these two notable properties has suggested to us the use of cerium doped zirconium titanate as an advanced support for thermal- and photocatalysis. Actually, by decorating the Ce_x-ZT powders with Pd we expect to trigger the same synergistic effects observed in the Pd/CeO_2 systems, which represent the state of the art among catalysts for the low temperature CO oxidation.[18]

2. Results and Discussion

2.1. Formation and Characterization of the Pd_y-Ce_x-ZT Catalysts

The Ce_x-ZT powders were investigated by some of us in previous works[17a] and consist of a solid solution of titania and zirconia ($ZrTiO_4$) with the structure of scrutinyite, typical of α-PbO_2, where the cerium cations occupy substitutional positions, either in the Ce(III) or Ce(IV) oxidation state. For an increasing amount of ceria, and in particular, at 10% loading, a small amount of pure ZrO_2 phase starts to segregate, setting a limit to the amount of cerium that can be introduced in the samples. It has been demonstrated by electron paramagnetic resonance (EPR) studies that the Ce(III)/Ce(IV) redox couple can activate molecular oxygen as superoxide radical anion $O_2^{\bullet-}$, making this solid solution a quite interesting material for redox reactions and in particular oxidations.[17b] In the following, we will focus on the characterization of the materials after the decoration with Pd nanoparticles (NPs) and on the study of the resulting catalytic properties.

In order to evaluate the permanent porosity of the Pd_y-Ce_x-ZT materials, N_2 adsorption experiments were performed at 77 K. The surface area deduced (**Figure 1**a and Figure S1–S5, Supporting Information) from the N_2 adsorption isotherms are 65, 62, 50, and 53 m^2 g^{-1} for Ce_{10}-ZT, $Pd_{0.4\%}$-Ce_{10}-ZT, $Pd_{2\%}$-Ce_{10}-ZT,
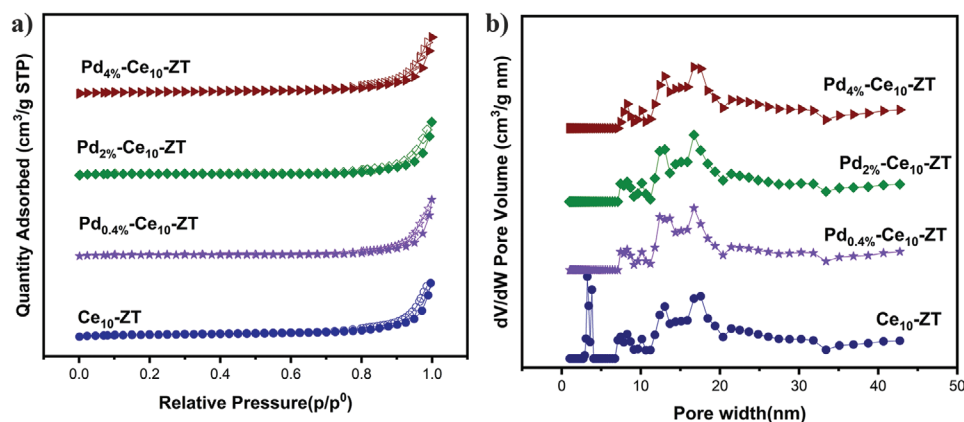
Figure 1. a) N_2 adsorption/desorption isotherms of the samples and b) pore size distribution of the samples.

**ADVANCED
SCIENCE NEWS**

www.advancedsciencenews.com

**ADVANCED
MATERIALS
INTERFACES**

www.advmatinterfaces.de

and $Pd_{4\%}$-Ce_{10}-ZT and 43, 33, 39, and 34 m^2 g^{-1} for Ce_8-ZT, $Pd_{0.4\%}$-Ce_8-ZT, $Pd_{2\%}$-Ce_8-ZT, and $Pd_{4\%}$-Ce_8-ZT, respectively. As reported previously, the cerium doping is responsible for an increase of the surface area because it leads to the formation of smaller NPs. Obvious hysteresis loops in N_2 adsorption–desorption isotherms with a type IV behavior were observed in all cases, with the P/P^0 position of the inflection point corresponding to a pore diameter in the mesoporous range. The adsorption experiments indicate that after the impregnation with Pd, the specific surface area of Pd_y-Ce_x-ZT decreases, possibly because of the partial pore blocking due to the introduction of the metal species. Moreover, applying a Density Functional Theory model, we determined the pore size distributions, indicating that these samples possess a mesoporous structure (Figure 1b and Figure S2–S6, Supporting Information). Notably, the pore size smaller than 5 nm disappeared after the impregnation with the Pd salt.

The powder X-ray diffraction (XRD) is an excellent tool to confirm the NPs formation, stability of the support and possible formation of additional phases. The representative XRD patterns of pure Ce_{10}-ZT, $Pd_{0.4\%}$-Ce_{10}-ZT, $Pd_{2\%}$-Ce_{10}-ZT, $Pd_{4\%}$-Ce_{10}-ZT and pure Ce_8-ZT, $Pd_{0.4\%}$-Ce_8-ZT, $Pd_{2\%}$-Ce_8-ZT, $Pd_{4\%}$-Ce_8-ZT are shown in **Figure 2** and Figure S7 in the Supporting Information together with the simulated pattern of the parent ZT compound for comparison.[19] The absence of CeO_2 related diffraction peaks lines is due to the efficient incorporation of Ce cations as substitutional species. Moreover, after the Pd impregnation, no Pd related diffraction features were detected. XRD patterns of the $Pd_{0.4\%}$-Ce_{10}-ZT, $Pd_{2\%}$-Ce_{10}-ZT, $Pd_{4\%}$-Ce_{10}-ZT displayed only diffraction peaks associated with the Ce_{10}-ZT support regardless of the metal content in the materials, probably due to the extremely low Pd content in the catalysts which could be under the detection limit of XRD technique. The crystal size of the Ce_{10}-ZT NPs is 18 nm according to Scherrer Equation. Along with their XRD patterns, the visual color change of the Ce_{10}-ZT crystals after deposition Pd NPs was also provided in Figure 2. The light yellow of the Ce_{10}-ZT sample changes to dark grey after reduction indicating the formation of Pd NPs.

Diffuse reflectance spectra acquired on the Pd_y-Ce_x-ZT powders (Figure S8, Supporting Information) indicate the presence of clear absorption tail in the range between 350 and 450 nm, which is due both to Ce induced levels and to localized surface plasmon resonance connected to the presence of Pd NPs.

Actually the sample with the highest absorption results to be $Pd_{4\%}$-Ce_{10}-ZT. Tauc's plot analysis on the other hand does not show significant differences in the value of the band gap compared to the undoped ZT powder (3.8 eV, Figure S9, Supporting Information).

The morphological properties of the catalysts were investigated by scanning electronic microscopy (SEM) and transmission electron microscopy (TEM). Figures S10–S13 in the Supporting Information show that bare Ce_{10}-ZT and Ce_8-ZT samples are composed of small (around 18–27 nm) crumb-like particles that are often densely aggregated. The particle size determined by electron microscopy is in agreement with the value derived from XRD patterns. After Pd deposition, the morphology is substantially preserved, which indicates that Pd NPs were homogeneously distributed on the surface of Ce_{10}-ZT and Ce_8-ZT without forming any appreciable separated aggregate. The low-magnification TEM images presented in Figures S12 and S13 in the Supporting Information, suggest that all catalysts display agglomerated NPs, but no significant difference is observed as a function of composition (i.e., Ce doping). To observe the morphological details of the catalysts, high-resolution TEM images were taken (**Figure 3** and Figure S14 and S15, Supporting Information). The oxide NPs are highly crystalline and their lattice planes can be easily recognized, confirming the formation of the scrutinyite polymorph. To confirm the presence of Pd nanoparticles dispersed on the ZT-based matrix, the lattice spacing of two different areas, previously correlated with the doped Ce-doped ZT support (orange square) and Pd NP (violet square), was calculated by applying fast Fourier transform (FFT) (Figure S15b,c, Supporting Information) to visualize the diffraction pattern. After selecting specific diffraction spots, Inverted FFT images (Figure S15d,e, Supporting Information) allow determining d-spacings by using the square plots (inset in Figure S15d,e, Supporting Information). According to the analysis reported in Figure S15 in the Supporting Information, a d-spacing of ≈2.39 Å was determined (violet panel), which corresponds to the (111) planes of Pd. A value of 3.07 Å was found for the orange selected area, which can be assigned to (111) family planes of the CeO_2 -ZrO_2/TiO_2 system. The same information could be obtained also by the direct measurements of the lattice fringe in high resolution TEM (HR-TEM) images like those reported in Figure S14 in the Supporting Information.
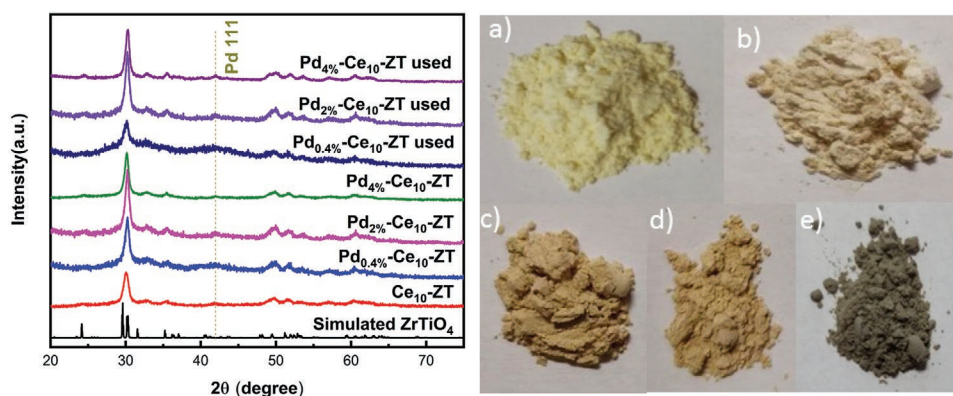

Figure 2. (Left) Powder XRD patterns of the different catalysts and (right) the color of the samples a) Ce_{10}-ZT, b) $Pd_{0.4\%}$-Ce_{10}-ZT, c) $Pd_{2\%}$-Ce_{10}-ZT, d) $Pd_{4\%}$-Ce_{10}-ZT, and e) $Pd_{2\%}$-Ce_{10}-ZT after H_2 activated.

ADVANCED
SCIENCE NEWS
www.advancedsciencenews.com

ADVANCED
MATERIALS
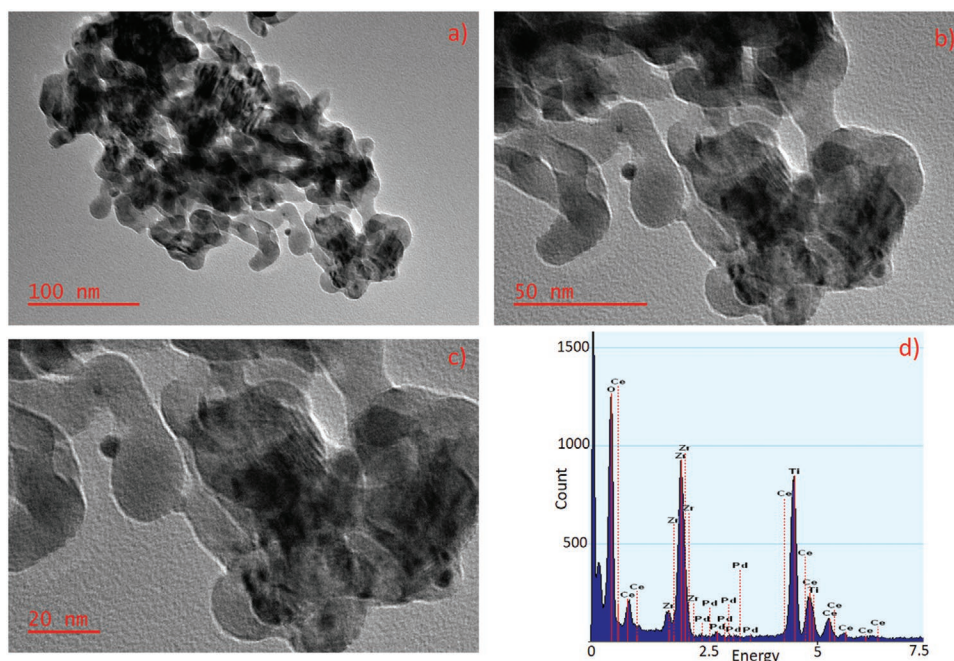**INTERFACES**
www.advmatinterfaces.de

Figure 3. a–c) TEM images acquired at different magnifications. d) Representative EDX spectrum acquired on three different zones of the particle here visualized.

Identification and distributions of Pd nanoparticles, have been further evaluated by combining micrographies and energy-dispersive X-ray spectroscopy (EDX) spectroscopy. As emerged from Figure 3a–c, the presence of Pd NPs is revealed by their contrast and regular shapes with respect to the support. Furthermore, EDX spectra acquired on several particles (see Figure 3d as representative one) disclosed the presence of Pd (1.09 wt%, in the sample $Pd_{2\%}$-Ce_{10}-ZT) and other elements reported in Table S1 in the Supporting Information. The compositional values have been also confirmed by EDX data acquired on micrometric regions with an SEM instrument. For all samples the actual amount of Pd was 50% of the nominal weight percentage, whereas Cerium concentration was in accordance with the molar ratio used for the synthesis.

The dimensions of the so-identified Pd NPs were comprised between 6.9 and 9 nm. No phase-separated structures related to ceria could be observed confirming that Ce cations are substitutionally incorporated into the ZT lattice.

XPS was used to determine the composition of the samples and the chemical state of the metal decorated oxides. As an example, the Pd 3d and Ce 3d photoemission spectra of the catalysts $Pd_{2\%}$-Ce_{10}-ZT are shown in **Figure 4**, but similar results can be obtained also for samples with different Pd loading and Cerium doping (see Figures S16–S21, Supporting Information).[20] The Pd 3d photoemission spectrum consists of a doublet corresponding to the Pd $3d_{5/2}$ and Pd $3d_{3/2}$ peaks, respectively, which is superimposed to the much more intense photoemission line of Zr 3p levels, therefore to separate the two signals it was necessary a fitting procedure. As shown in Figure 4a, after Pd deposition, two peaks at a binding energies (BE) position of 335.7 and 341 eV can be observed, which can be attributed to ultrasmall metal NPs, demonstrating that the

Pd(II) cations in the K_2PdCl_4 precursor could be reduced to Pd(0) during the hydrogen treatment.[21] Due to the very low intensity of the Pd signal, we cannot exclude the presence of oxidized PdO_x species, which some authors associate with high catalytic activity at low temperature.[22] The complex spectrum of Ce 3d was decomposed using ten single peaks as outlined in Figure 4b. The two sets of spin–orbit doublets, which correspond to the $3d_{3/2}$ and $3d_{5/2}$ peaks, were labeled u and v, respectively; two doublets are ascribed to Ce(III) and three to Ce(IV).[23] The existence of distinct doublets for each ion is due to final state effects consisting of an electron transfer from oxygen to cerium, producing different final state configurations.[24] From the fit we could deduce the ratio between Ce(III)/Ce(IV) (Table S2, Supporting Information). We can notice that in all Ce_x-ZT samples the amount of Ce(III) species increased after the loading Pd, for example passing from 42% in Ce_{10}-ZT to 55% in $Pd_{2\%}$-Ce_{10}-ZT. This suggests the existence of a charge transfer between the Pd NPs and the oxide support, which can effectively store electrons in the Ce 4f levels. This correlation between Pd NPs and Ce(III) is extremely interesting. Actually, in a previous work it has been demonstrated that Ce(III) cation in zirconium titanate can interact with molecular oxygen and produce (98%) weakly bonded superoxides species, which are known to be key intermediates in the CO oxidation reaction.[17b] On the other hand, the Zr 3d and Ti 2p spectra photoemission spectra do not show any change after the deposition of palladium and the detected amount of reduced species is negligible (Figures S22–S25, Supporting Information). These results are in agreement with previous works on the same materials, which showed that the 4f levels of ceria are lower in energy of both Ti 3d and Zr 4d states, therefore are preferentially populated, determining the selective formation of large amount of Ce(III) species.[17a]
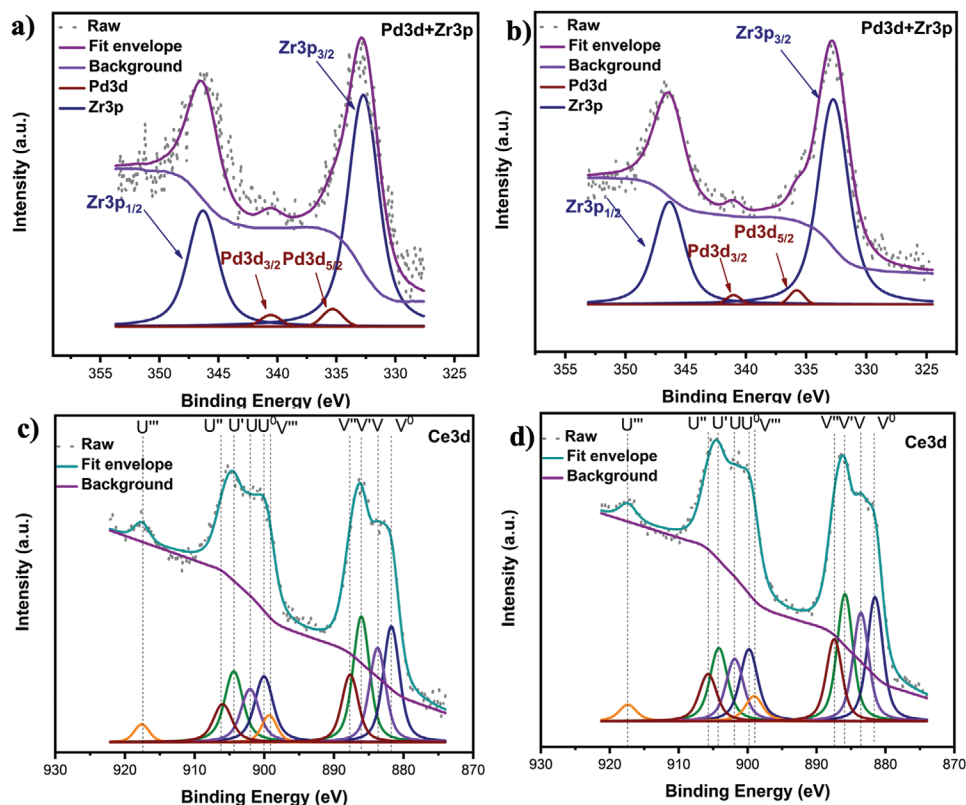
Figure 4. a,c) Pd 3d and Ce 3d photoemission spectra of $Pd_{2\%}$-Ce_{10}-ZT and b,d) Pd 3d and Ce 3d XPS spectra of $Pd_{2\%}$-Ce_{8}-ZT.

2.2. Catalytic CO Oxidation on Pd_y-Ce_x-ZT Catalysts

The selective oxidation of CO is one of the most important transformations in chemistry, with a notable impact on practical applications whenever the combustion of organic compounds is involved, but also for fundamental studies, where given its simplicity, it is usually exploited as a model reaction.[25] A wide range of oxide supported transition metal NPs have been extensively utilized for this reaction outlining complex synergies between the metal and the metal oxide, especially when reducible supports are involved.[26] In order to understand the fundamental chemistry of our multicomponent Pd_y-Ce_x-ZT nanocatalysts we started from the investigation of both the ternary oxide supports without palladium and of single components oxides (e.g., CeO_2, ZrO_2) supporting different amounts of metal. First, we investigated the CO oxidation reaction at different temperatures (thermocatalysis) and then the improvement of the performance induced by light irradiation (photocatalysis).

In the case of the binary (ZT) and ternary (Ce-ZT) oxides without Pd (Figure S26, Supporting Information), it can be seen that the catalytic activity is very low and full conversion is not achieved even at 300 °C, when the conversion is only 1%, 1%, and 1.4% for ZT, Ce_8-ZT, and Ce_{10}-ZT, respectively (details in inset Figure S28, Supporting Information). Anyway, the best CO oxidation performance is observed on the Ce_{10}-ZT sample, suggesting that the presence of cerium dopants is beneficial for catalytic activity.

The introduction of palladium clearly boosts the catalytic performance. For pure ZrO_2, no matter how much Pd is added, the full conversion temperature is achieved at 140 °C. On the other hand, for CeO_2, the full conversion temperature decreases from 120 to 100 °C as the Pd loading is increased from 0.4% to 4% (Figures S27 and S28, Supporting Information). These data suggest that palladium is the active phase for CO oxidation, but its activity can be variably modulated by the oxide support and in particular by the interaction with ceria. Therefore, we investigated in detail the effect of palladium and cerium loading on the catalytic activity of the Pd_y-Ce_x-ZT samples. **Table 1** summarizes the light-off temperatures at full ($T_{100\%}$) and 50% conversion ($T_{50\%}$) of the different catalysts, whereas **Figure 5** shows the single light-off curves of each sample from room temperature up to 300 °C. The same heating and cooling cycles were applied to the whole set of catalysts.

Interestingly the oxide support with the highest ceria concentration (10% molar ratio, Ce_{10}-ZT) has the best performance for a certain loading of palladium and it is also more performing even than pure CeO_2 with similar physicochemical properties (surface area and crystallinity, Figure S29, Supporting Information). The better performance of Ce_{10}-ZT compared to CeO_2 is likely connected to the fact that as dopants in ZT, given the special electronic structure of the host, the cerium species can be easily and reversibly reduced to Ce(III) cations (see Table S2, Supporting Information), which are the real active species assisting the CO oxidation providing highly active oxygen species in the form of superoxide ions.[17b,27]

The amount of palladium is the other key parameter for the CO oxidation (Figures S30–S32, Supporting Information). By inspecting the data in Table 1, it can be observed that in most

Table 1. Temperature (°C) of partial (50%) and total (100%) CO conversion.

Catalysts	$T_{50\%}$ [°C]	$T_{100\%}$ [°C]	CO_2 selectivity [%]
$Pd_{0.4\%}$-ZT	168	180	>99
$Pd_{2\%}$-ZT	113	120	>99
$Pd_{4\%}$-ZT	93	100	>99
$Pd_{0.4\%}$-Ce_8-ZT	93	100	>99
$Pd_{2\%}$-Ce_8-ZT	63	70	>99
$Pd_{4\%}$-Ce_8-ZT	73	80	>99
$Pd_{0.4\%}$-Ce_{10}-ZT	72	80	>99
$Pd_{2\%}$-Ce_{10}-ZT	45	50	>99
$Pd_{4\%}$-Ce_{10}-ZT	55	60	>99

cases a higher Pd loading produces lower $T_{50\%}$ and $T_{100\%}$ temperatures. The effect is very remarkable for pure oxides, whereas in the case of the Ce-ZT ternary oxides on passing from Pd 0.4% to Pd 2% we observed an increase of the activity, whereas further addition of Pd (4%) does not produce a significant improvement: probably, after the initial increase of the number of active sites due to the increase of Pd loading, a further metal addition leads only to the enlargement of pre-existing NPs, with a limited effect on the catalytic activity. Overall, the best catalyst is $Pd_{2\%}$-Ce_{10}-ZT that exhibits a $T_{50\%}$ of 45 °C and a $T_{100\%}$ of 50 °C, which in terms of time over frequency (TOF) corresponds to a value of 0.05 s^{-1} at 45 °C. However, if we consider that both TEM and SEM EDX data indicate that the actual Pd loading on $Pd_{2\%}$-Ce_{10}-ZT is only 1%, the true TOF becomes 0.1 s^{-1}. These values are excellent compared to other similar catalytic systems consisting of noble metals supported on oxides (see Table S3, Supporting Information).

The durability of $Pd_{2\%}$-Ce_{10}-ZT was investigated by repeating several light-off experiments with the same sample (Figures S33 and S34, Supporting Information). The results demonstrated that there is no significant decrease in catalytic activity after three runs for all samples, indicating that they are rather stable and no poisoning phenomena such as overoxidation of the metal phase or coke deposition take place, as confirmed by Raman spectroscopy (Figures S35 and S36, Supporting Information). The crystallinity of the Pd_y-Ce_x-ZT host matrix remained almost unchanged after the catalytic work, as shown

in Figure 2 and Figure S10 in the Supporting Information. SEM and TEM images of Pd_y-Ce_x-ZT before and after the CO oxidation revealed no change in the particle size distribution, and absence of sintering of Pd NPs as shown in Figures S11–S13 in the Supporting Information. HR-TEM further demonstrated the Pd NPs do not aggregate and their size remains peaked around 7 nm, as shown in Figure S14 in the Supporting Information. As illustrated in Figure S30 in the Supporting Information, We also tested at full conversion (i.e., at 50 °C) as a function of time the best catalysts, $Pd_{2\%}$-Ce_{10}-ZT, which maintained full conversion without any decrease of activity for 24 h.

According to previous literature, Ce_x-ZT has a good optical absorption in the UV and visible region,[17a] which, given the additional presence of small metal NPs, is further boosted as confirmed by our diffuse reflectance measurements (Figure S8, Supporting Information). Based on this idea, the Pd_y-Ce_x-ZT powders were used for photocatalytic CO oxidation. In this case to allow an efficient irradiation and easy thermalization of the sample, high gas flux and small amount of catalysts were used, operating at a very high space velocity (48 000 h^{-1}). Even with these precautions, the temperature of the samples was rising under illumination of about 5–8 °C, so in this case the experiments were started from 40 °C.

The experimental results clearly showed that the activity of CO oxidation increased under light irradiation. As shown in **Figure 6**, the samples the $Pd_{2\%}$-$Ce_{0.5}$-ZT and $Pd_{2\%}$-Ce_{10}-ZT achieved the catalytic activity of dark conditions at a temperature 40 °C lower under light irradiation. In the case of the sample $Pd_{2\%}$-Ce_8-ZT, the white light produces a downshift of 20 °C in the catalytic activity. Notably, the sample $Pd_{2\%}$-Ce_{10}-ZT, which is the best performing catalyst, under white light reaches the maximum catalytic activity already at near ambient conditions, at 40 °C, whereas at the same temperature in dark conditions is substantially inactive, the corresponding CO_2 production is shown in Figures S37–S40 in the Supporting Information. On the other hand, the activity of Ce_{10}-ZT showed no difference with or without white light, probably because the lack of an easy adsorption site for CO (i.e., metal palladium) is in any case suppressing the reaction (Figure S41, Supporting Information). Moreover, we performed photocatalytic measurements with a green light (533 nm, 89 mW cm^{-2}), i.e., in a region where the Ce_x-ZT oxide support does not directly absorb. In this case, we observed that most active catalysts ($Pd_{2\%}$-Ce_8-ZT and
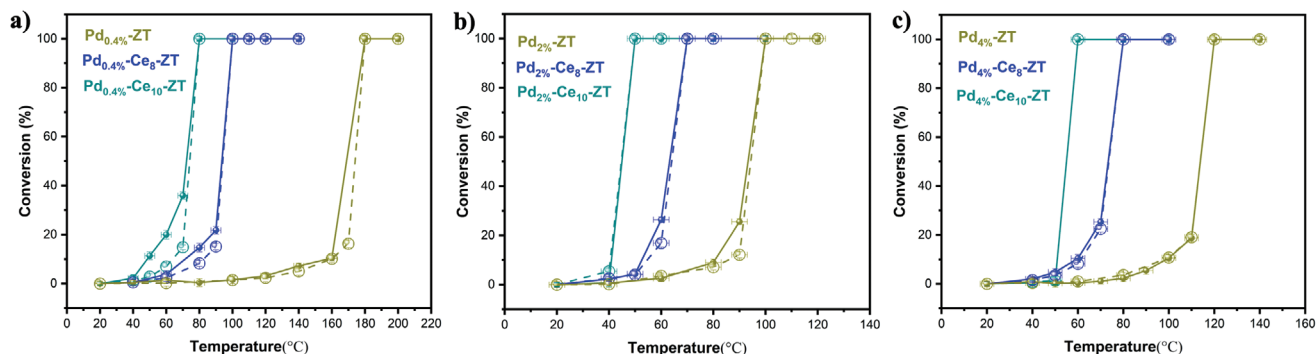

Figure 5. CO conversion versus temperature for different Ce concentration and Pd loading: a) Pd 0.4%, b) Pd 2%, c) Pd 4%; (filled dots, initial ramp with increasing temperature; empty dots, return from high to low temperature).
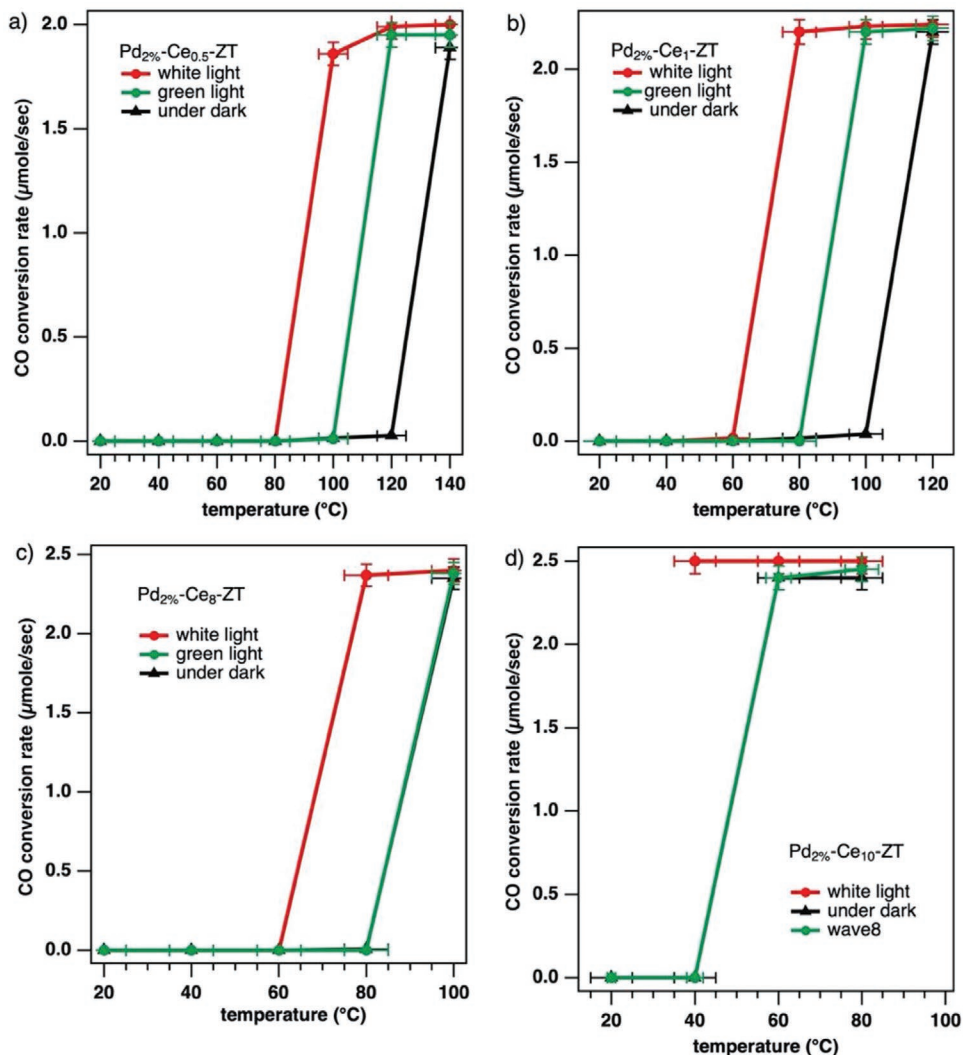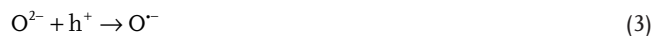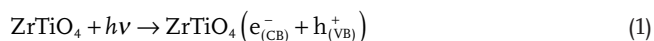
ADVANCED
SCIENCE NEWS
www.advancedsciencenews.com

ADVANCED
MATERIALS
INTERFACES
www.advmatinterfaces.de

Figure 6. CO light-off spectra of the different catalysts in dark condition (black traces) and under white (red traces) or green light (green traces). a) Pd2%-Ce0.5-ZT; b) Pd2%-Ce1-ZT; c) Pd2%-Ce8-ZT; d) Pd2%-C10-ZT.

Pd$_{2\%}$-Ce$_{10}$-ZT) did not improve the activity compared with dark conditions, while in the case of the least active catalysts (i.e., with low cerium amount), there was a modest enhancement of the catalytic performance under green light irradiation. Such promotion effect completely disappears in absence of Pd NPs. Overall these data suggest that the best catalytic activity is observed when the light can directly excite Ce 3d states because the Ce 3d sited are associated with the formation of active species (vide infra), but a small activity is also associated with the local surface plasmon resonance of the metal NPs.

In order to investigate the role of the irradiation on the CO oxidation mechanism, the catalysts were characterized via EPR. The effects of light irradiation on a photoactive system as the ZrTiO$_4$ in fact is the formation of charge carriers (photogenerated electrons end electron holes), which in turn can be trapped by the lattice ions forming paramagnetic species, according to reactions below reported (Equations (1)–(3)).[28] Previous work has also shown that the presence of Ce ion can affect the charge carriers separation since Ce^{4+} can act as

selective trapping sites for photoexcited electrons (Equation (4)) making simultaneously the photogenerated holes more available for surface oxidation processes.[17a]

$$ZrTiO_4 + h\nu \rightarrow ZrTiO_4 \left(e^-_{(CB)} + h^+_{(VB)} \right) \quad (1)$$

$$Ti^{4+}/Zr^{4+} + e^-_{(CB)} \rightarrow Ti^{3+}/Zr^{3+} \quad (2)$$

$$O^{2-} + h^+ \rightarrow O^{\bullet -} \quad (3)$$

$$Ce^{4+} + e^-_{(CB)} \rightarrow Ce^{3+} \quad (4)$$

In **Figure 7** we compared spectra acquired in dark and after 300 s irradiation for two samples with different Ce doping (0.5% and 10%) and with or without Pd NPs (2% w/w). Both samples show a weak signal due to trapped holes (O$^{\bullet -}$) and tiny amounts of Zr^{3+} defects in the starting material. The EPR
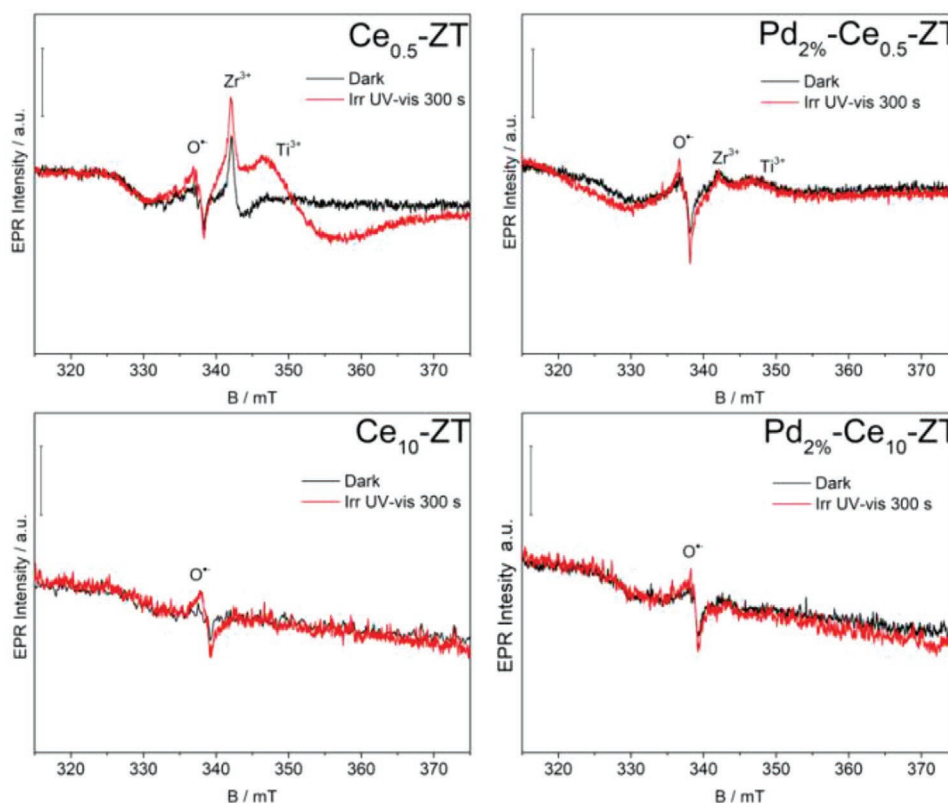
**ADVANCED
SCIENCE NEWS**

www.advancedsciencenews.com

**ADVANCED
MATERIALS
INTERFACES**

www.advmatinterfaces.de

Figure 7. EPR spectra of the samples Ce$_{0.5}$-ZT and Ce$_{0.5}$-ZT and the corresponding Pd loaded samples (Pd$_{2\%}$-Ce$_{0.5}$-ZT, Pd$_{2\%}$-Ce$_{10}$-ZT) before and after 300 s UV–vis irradiation.

data demonstrate that Ce(IV) and Pd NPs can both act as electron traps. Comparing the spectra acquired for both the samples with low or high Ce doping without Pd (sample Ce$_{0.5}$-ZT and Ce$_{10}$-ZT), it can be observed a remarkable suppression of the expected signal due to Ti^{3+} and Zr^{3+} species in the Ce$_{10}$-ZT sample. When Pd is also present no significant differences can be observed before and after irradiation for both Ce loading, indicating that the palladium further contributes to trapping the electrons. This effect is particularly clear in the sample containing the lower amount of cerium, in Ce$_{0.5}$-ZT material in fact, upon UV–vis irradiation the spectrum of the signal of Zr^{3+} slightly increases and simultaneously a very broad signal due to Ti^{3+} appears, indicating that the expected trapping of photoexcited electrons still occurs because of the low cerium concentration. Conversely, moving to the sample containing palladium (sample Pd$_{2\%}$-Ce$_{0.5}$-ZT) no significant differences are observed before or upon irradiation. Previously, it was also demonstrated that, at the gas-solid interface, in the Ce$_x$-ZT system the electron stored in the Ce^{3+} cations could be easily transferred to adsorbed O$_2$ molecules and generate superoxides species.[17b,29]

In order to confirm directly the generation of superoxides species (O$_2^{\bullet-}$) upon irradiation, EPR spectra of the Pd$_{2\%}$-Ce$_{10}$-ZT sample after irradiation in presence of air with visible light (white light emitting diode (LED)) or UV–vis light were recorded (Figure S42, Supporting Information). Before the irradiation step, recording the EPR spectra under vacuum at low temperature (77 K), no signal due to paramagnetic centers was observed

(black line). On the contrary, in the same conditions after light irradiation of the sample in contact with air, an EPR signal was observed, and two species could be identified: the first one characterized by a **g** tensor whose principal values are $g_1 = 2.030$ and $g_2 = 2.011$ and the second one recognizable by the component at $g = 2.003$. The first species dominates the spectrum and similar signals are reported for CeO$_2$ and the Ce containing systems, therefore it can be unambiguously assigned to the superoxide species adsorbed on Ce^{4+} ions hosted in the ZrTiO$_4$ lattice (O$_2^{\bullet-}$—Ce^{4+}).[17,29,30] The second one, weaker and partially buried in the previous signal is the evidence of superoxide species adsorbed on the tetravalent ions of the zirconium titanate lattice (O$_2^{\bullet-}$—Ti^{4+}/Zr^{4+}).[31,32] This last species is characterized by a orthorhombic symmetry of the **g** tensor ($g_{xx} < g_{yy} \ll g_{zz}$) and in the present case only the lower component ($g_{xx} \equiv g = 2.003$) can be clearly observed.

The observed photocatalytic contribution to the CO oxidation process therefore can be explained assuming that photoexcited electrons are quickly trapped into Ce^{3+} cations or even Pd NPs, where they are able to form superoxide species through reaction with adsorbed oxygen species. Then the superoxide anions can react with the CO adsorbed on Pd NPs or even directly with the CO$^+$ species activated by the holes remaining in the valence band of the oxide.[33] A similar photothermocatalytic effect has been previously reported also for the oxidation of benzene operated by TiO$_2$/CeO$_2$ nanocomposite.[34] In that case, however, the improved catalytic performance was traced back to a synergistic combination of photocatalytic effect on TiO$_2$, which provided

activated oxygen species and thermocatalysis on CeO_2, which under irradiation enhanced its reducibility, and therefore it was localized specifically at the interface between the two oxides. In the present case on the other hand, the homogeneous cerium doping into the zirconium titanate host, synergistically realizes both function: being involved in the light adsorption and generation of oxygen species and being strongly stabilized in a reduced oxidation state.

3. Conclusion

In this work, novel Ce_x-ZT ternary oxides were employed as advanced supports for Pd NPs and used as catalysts for the CO oxidation reactions. These novel materials demonstrated to be more active than the corresponding undoped single phases, zirconium titanate, CeO_2, and ZrO_2.

The amount of Ce doping and Pd loading both played an important role in the improvement of the catalytic activity. The best catalyst was the sample with a nominal 2% w/w of Pd and 10% molar doping of cerium, which was able to achieve complete CO conversion even at 50 °C and maintained such outstanding performance for several light-off experiments or more than 24 h at full conversion conditions. Such excellent catalytic activity has been associated with the high reducibility of cerium atoms that can be easily stabilized as Ce(III) species within the zirconium titanate host. The Ce loading did not affect only the redox properties but also conferred light absorption properties in the visible range and therefore photoactivity. Actually, catalytic tests carried out under illumination with a white led demonstrated a significant improvement of the catalytic performance. EPR experiments suggested that both Pd NPs and Ce (IV) ions act as electron traps and eventually transfer the electrons to oxygen molecules and form superoxide species.

This work exemplifies the great potential of doped mixed oxides as supports for catalysis. Even though key materials properties such as surface area, morphology, porosity, and dispersion of the active phase have not been optimized, still the catalytic performance was excellent, much higher than other Pd catalysts supported on standard oxides. Additional work is necessary to further improve the catalytic activity in the CO oxidation as well as to tailor the optical absorption properties in the visible range in order to boost the photoactivity. Nonetheless to design solid solutions of reducible oxides in such a way that catalytic active species (in this case Ce(III)) can be selectively stabilized, holds great promise and can definitely stimulate more research work oriented to the design of a new family of sustainable catalysts, to be used in other photoreactions or advanced oxidations.

4. Experimental Section

Samples Preparation—Synthesis of Ce$_x$-ZT: According to a previously reported procedure,[17a,28] pristine $ZrTiO_4$ powders (hereafter ZT) were prepared through a sol–gel route, mixing a solution of 3.5 mL of titanium(IV) isopropoxide and 5 mL of zirconium(IV) propoxide (molar ratio 1:1) in 9 mL of 2-propanol and adding 3.5 mL of water. The gel was aged for 15 h at 290 K, and dried at 343 K. Then, the dried material was calcined in air at 973 K for 1 h, obtaining a white colored powder.

Ce doped-$ZrTiO_4$ powders (hereafter called Ce$_x$-ZT where x is the Ce molar ratio in the mixed oxide), were prepared in a similar manner, just adding to the previous precursor solution, 3.5 mL of water solution of $CeCl_3 \cdot 7H_2O$ in order to have different molar ratios of cerium (from 0.5 to 10 mol%, Table 1). Aging, drying, and thermal treatment were the same as for undoped materials. The resulting powder showed a yellow color, more vivid in the case of the Ce_{10}-ZT sample.

Samples Preparation—Synthesis Pd Decorated Ce$_X$-ZT: Different amounts of Pd were loaded on the Ce$_x$-ZT NPs by a simple impregnation technique.[35] A certain quantity of (K_2PdCl_4), 1 mg, 5 mg, and 10 mg, was dissolved with 5 mL of water, then 80 mg Ce$_x$-ZT were added. The mixture was aged at room temperature (RT) for 48 h, and then calcined in a tube furnace at 450 °C in air for 4 h to obtain Pd$^{(II)}_y$-Ce$_x$-ZT. In situ reduction of the catalysts in H_2 at 200 °C for 2 h was performed to obtain the desired metallic Pd NPs. The final material was labeled Pd$_y$-Ce$_x$-ZT, where y is the nominal mass percentage of Pd on the Ce$_x$-ZT (1 mg = 0.4%, 5 mg = 2%, and 10 mg = 4%).

Evaluation of the Catalytic Activity: The evaluation of catalytic activity was carried out in a continuous flow, fixed-bed quartz tubular reactor (inner diameter: 4 mm). To allow an efficient gas diffusion, the catalyst powder was dispersed on quartz wool. Prior to all catalytic tests, the sample (50 mg) was activated in a flow of 20 vol% hydrogen diluted with nitrogen at 200 °C for 1 h (total flow rate 50 mL min^{-1}) as a standard pretreatment. Gas flow rates were controlled by mass flow controllers. After the activation, the sample was cooled down to room temperature and exposed to the reaction mixture (CO: 1.8 sccm, O_2: 1.8 sccm, and N_2 balanced to 50 mL min^{-1}, space velocity of 15 000 h^{-1}) at different temperature (from RT to 300 °C). Product analysis was carried out online with a Agilent 490 micro-gas chromatograph equipped with a thermal conductivity detector. Two columns were used in parallel: a Molsieve 5A column to quantify O_2 and CO, and a PoraPLOT Q column to quantify CO_2. Both columns were operated at 110 °C.

The total conversion was defined as the CO conversion

$$X_{total} = X_{CO} = \frac{n_{CO}^{in} - n_{CO}^{out}}{n_{CO}^{in}} \times 100 (\%) \tag{5}$$

Oxygen consumption can be defined as

$$X_{O_2} = \frac{n_{O_2}^{in} - n_{O_2}^{out}}{n_{O_2}^{in}} \times 100 (\%) \tag{6}$$

Photocatalysis experiments were carried out in a planar fixed bed reactor. A white LED with a power of 90 mW cm^{-2} was used to illuminate the sample through a SiO_2 window (see Figure S43, Supporting Information, for the emission spectrum of the LED). An amount of 10 mg of catalyst was dispersed with silica wool inside a ceramic heater that was in contact with a thermocouple. The reaction mixture in this case was containing 5 sccm CO, 1.8 sccm O_2 and balanced to a total of 50 mL min^{-1} with N_2. In this photoreactor the space velocity was very high, 48 000 h^{-1}.

Characterizations: X-ray photoelectron spectroscopic (XPS) analysis was performed to examine the composition of the samples. The BE were calibrated internally setting the position of the peak of adventitious carbon in the C 1s spectrum at an energy of 284.6 eV. The powder XRD patterns were obtained with a PANalytical PW3040/60 X'Pert PRO MPD camera with Cu K_{a1}-radiation (l = 1.54056 A° 40 KV, and 100 mA). The intensities were obtained in the 2θ range between 20° and 80°. The morphology of the samples was obtained with a Zeiss Supra VP35 SEM, equipped with an EDX for element analysis. High-resolution TEM observations were performed using a JEM-2100F system or an FEI TECNAI 200 operating at 200 kV working with a field emission electron gun. Surface area, pore volume, and pore size distribution were measured by nitrogen adsorption/desorption at 77 K using a Micromeritics ASAP 2020. The samples were degassed at 120 °C for 12 h before the adsorption experiments. The surface area (S_{BET}) was determined by Brunauer–Emmett–Teller

(BET) method in the 0–0.9 partial pressure range and the pore size distribution was determined by the density functional theory method from the desorption branch of the isotherm.[36] Continuous wave electron paramagnetic resonance experiments were performed with a Bruker EMX spectrometer operating at X-band (9.5 GHz), equipped with a cylindrical cavity operating at 100 kHz field modulation. The samples were investigated in vacuum after outgassing at RT (residual pressure $P < 10^{-4}$ mbar) at the liquid nitrogen temperature (77 K). Spectra upon irradiation were obtained irradiating the materials directly in the EPR cavity at 77 K using a 1600 W Hg lamp (Newport Instruments) with a light beam output set at 1000 W and equipped with an IR water filter.

Supporting Information

Supporting Information is available from the Wiley Online Library or from the author.

Acknowledgements

Conflict of Interest

The authors declare no conflict of interest.

Data Availability Statement

Research data are not shared.

Keywords

[1] T. P. Beebe, P. Gelin, J. J. T. Yates, *Surf. Sci.* **1984**, *148*, 526.

[2] a) H. Li, M. Shen, J. Wang, H. Wang, J. Wang, *Ind. Eng. Chem. Res.* **2020**, *59*, 1477; b) T. Osaki, *Mater. Res. Bull.* **2019**, *118*, 110498.

[3] a) T. Zhang, S. Wang, F. Chen, *J. Phys. Chem. C* **2016**, *120*, 9732; b) Y. Yang, Y. Li, M. Zeng, M. Mao, L. Lan, H. Liu, J. Chen, X. Zhao, *Appl. Catal., B* **2018**, *224*, 751.

[4] a) M. Jin, J.-N. Park, J. K. Shon, J. H. Kim, Z. Li, Y.-K. Park, J. M. Kim, *Catal. Today* **2012**, *185*, 183; b) S. Royer, D. Duprez, *ChemCatChem* **2011**, *3*, 24.

[5] S. Golunski, R. Rajaram, *CATTECH* **2002**, *6*, 30.

[6] a) F. M. S. Arrii, A. J. Renouprez, J. L. Rousset, *J. Am. Chem. Soc.* **2004**, *125*, 1199; b) X. Xie, Y. Li, Z. Q. Liu, M. Haruta, W. Shen, *Nature* **2009**, *458*, 746.

[7] F. M. Pinto, V. Y. Suzuki, R. C. Silva, F. A. La Porta, *Front. Mater.* **2019**, *6*, 260.

[8] A. Martínez-Arias, M. Fernández-García, O. Gálvez, J. M. Coronado, J. A. Anderson, J. C. Conesa, J. Soria, G. Munuera, *J. Catal.* **2000**, *195*, 207.

[9] M. Shen, M. Yang, J. Wang, J. Wen, M. Zhao, W. Wang, *J. Phys. Chem. C* **2009**, *113*, 3212.

[10] N. J. Lawrence, J. R. Brewer, L. Wang, T. S. Wu, J. Wells-Kingsbury, M. M. Ihrig, G. Wang, Y. L. Soo, W. N. Mei, C. L. Cheung, *Nano Lett.* **2011**, *11*, 2666.

[11] M. Coduri, S. Checchia, M. Longhi, D. Ceresoli, M. Scavini, *Front. Chem.* **2018**, *6*, 526.

[12] a) G. Zhou, L. Barrio, S. Agnoli, S. D. Senanayake, J. Evans, A. Kubacka, M. Estrella, J. C. Hanson, A. Martínez-Arias, M. Fernández-García, J. A. Rodriguez, *Angew. Chem., Int. Ed.* **2010**, *49*, 9680; b) L. Chen, Z. Si, X. Wu, D. Weng, *ACS Appl. Mater. Interfaces* **2014**, *6*, 8134; c) J. Graciani, J. J. Plata, J. F. Sanz, P. Liu, J. A. Rodriguez, *J. Chem. Phys.* **2010**, *132*, 104703; d) S. Agnoli, A. E. Reeder, S. D. Senanayake, J. Hrbek, J. A. Rodriguez, *Nanoscale* **2014**, *6*, 800; e) J. B. Park, J. Graciani, J. Evans, D. Stacchiola, S. Ma, P. Liu, A. Nambu, J. F. Sanz, J. Hrbek, J. A. Rodriguez, *Proc. Natl. Acad. Sci. U. S. A.* **2009**, *106*, 4975.

[13] a) T. X. T. Sayle, S. C. Parker, D. C. Sayle, *Chem. Commun.* **2004**, *21*, 2438; b) S. Deshpande, S. Patil, S. V. N. T. Kuchibhatla, S. Seal, *Appl. Phys. Lett.* **2005**, *87*, 133113; c) G. Spezzati, A. D. Benavidez, A. T. DeLaRiva, Y. Su, J. P. Hofmann, S. Asahina, E. J. Olivier, J. H. Neethling, J. T. Miller, A. K. Datye, E. J. M. Hensen, *Appl. Catal., B* **2019**, *243*, 36.

[14] L. Artiglia, S. Agnoli, M. C. Paganini, M. Cattelan, G. Granozzi, *ACS Appl. Mater. Interfaces* **2014**, *6*, 20130.

[15] J. R. Sohn, S. H. Lee, *Appl. Catal., A* **2004**, *266*, 89.

[16] G. Colón, M. Hidalgo, J. Navío, *Appl. Catal., A* **2002**, *231*, 185.

[17] a) V. Polliotto, E. Albanese, S. Livraghi, S. Agnoli, G. Pacchioni, E. Giamello, *Catal. Today* **2020**, *340*, 49; b) V. Polliotto, S. Livraghi, S. Agnoli, G. Granozzi, E. Giamello, *Appl. Catal., A* **2019**, *580*, 140.

[18] E. M. Slavinskaya, R. V. Gulyaev, A. V. Zadesenets, O. A. Stonkus, V. I. Zaikovskii, Y. V. Shubin, S. V. Korenev, A. I. Boronin, *Appl. Catal., B* **2015**, *166–167*, 91.

[19] S. A. Khan, S. B. Khan, A. M. Asiri, I. Ahmad, *Nanoscale Res. Lett.* **2016**, *11*, 345.

[20] F. Carraro, A. Fapohunda, M. C. Paganini, S. Agnoli, *ACS Appl. Nano Mater.* **2018**, *1*, 1492.

[21] a) X. Wang, J. Chen, J. Zeng, Q. Wang, Z. Li, R. Qin, C. Wu, Z. Xie, L. Zheng, *Nanoscale* **2017**, *9*, 6643; b) M. Blanco, D. Mosconi, C. Tubaro, A. Biffis, D. Badocco, P. Pastore, M. Otyepka, A. Bakandritsos, Z. Liu, W. Ren, S. Agnoli, G. Granozzi, *Green Chem.* **2019**, *21*, 5238.

[22] G. Spezzati, Y. Su, J. P. Hofmann, A. D. Benavidez, A. T. DeLaRiva, J. McCabe, A. K. Datye, E. J. Hensen, *ACS Catal.* **2017**, *7*, 6887.

[23] C. Zhang, J. Lin, *Phys. Chem. Chem. Phys.* **2011**, *13*, 3896.

[24] J. Seo, A. Gowda, S. V. Babu, *ECS J. Solid State Sci.* **2018**, *7*, 243.

[25] a) K. Mori, T. Hara, T. Mizugaki, K. Ebitani, K. Kaneda, *J. Am. Chem. Soc.* **2004**, *126*, 10657; b) Z. Hu, F. M. Kerton, *Appl. Catal., A* **2012**, *413–414*, 332.

[26] C. Parmeggiani, F. Cardona, *Green Chem.* **2012**, *14*, 547.

[27] J. Guzman, S. Carrettin, J. C. Fierro-Gonzalez, Y. Hao, B. C. Gates, A. Corma, *Angew. Chem., Int. Ed.* **2005**, *44*, 4778.

[28] V. Polliotto, E. Albanese, S. Livraghi, P. Indyka, Z. Sojka, G. Pacchioni, E. Giamello, *J. Phys. Chem. C* **2017**, *121*, 5487.

[29] a) S. Livraghi, M. C. Paganini, E. Giamello, G. Di Liberto, S. Tosoni, G. Pacchioni, *J. Phys. Chem. C* **2019**, *123*, 27088; b) C. Gionco, E. Giamello, L. Mino, M. C. Paganini, *Phys. Chem. Chem. Phys.* **2014**, *16*, 21438.

[30] J. Soria, A. Martinez-Arias, J. C. Conesa, *J. Chem. Soc., Faraday Trans.* **1995**, *91*, 1669.

[31] S. Livraghi, F. Olivero, M. C. Paganini, E. Giamello, *J. Phys. Chem. C* **2010**, *114*, 18553.

[32] E. Carter, A. F. Carley, D. M. Murphy, *J. Phys. Chem. C* **2007**, *111*, 10630.

[33] Y. Liu, X. Zhang, J. Bian, J. Sun, Z. Li, I. Khan, Y. Qu, Z. Li, Z. Jiang, L. Jing, *Appl. Catal., B* **2019**, *254*, 260.

[34] J. Biener, M. M. Biener, R. J. Madix, C. M. Friend, *ACS Catal.* **2015**, *5*, 6263.

[35] a) S. R. Mirmasoomi, M. Mehdipour Ghazi, M. Galedari, *Sep. Purif. Technol.* **2017**, *175*, 418; b) M. Su, Y. Fang, B. Li, W. Yin, J. Gu, H. Liang, P. Li, J. Wu, *Sci. Total Environ.* **2019**, *647*, 47.

[36] J. Landers, G. Y. Gor, A. V. Neimark, *Colloids Surf., A* **2013**, *437*, 3.